# 3D Arrays of 1024-Pixel Image Sensors based on Lead Halide Perovskite Nanowires

*Leilei Gu, Mohammad Mahdi Tavakoli, Daquan Zhang, Qianpeng Zhang, Aashir Waleed, Yiqun Xiao, Kwong-Hoi Tsui, Yuanjing Lin, Lei Liao, Jiannong Wang, and Zhiyong Fan**

Quasi-one-dimensional (Q-1D) semiconducting nanostructures, such as nanowires (NWs) and nanorods, provide guiding channels for transportation and propagation of charge carriers and photons in one dimension while confining them in the other two dimensions. This unique feature renders NWs intriguing electrical and optical properties, which are not only fundamentally interesting, but also technologically useful for a variety of device applications including transistors,[1,2] diodes,[3,4] memory,[5,6] sensors,[7–9] etc. Particularly for optoelectronics, NW-based photodetectors and photovoltaic devices have demonstrated high gain and high energy-conversion efficiency, either due to the prolonged carrier life-time or efficient light harvesting and carrier extraction.[10–12] The proper choice of materials is apparently crucial for rational design of a high-performance device. In fact, there is a wide range of choice of high-quality inorganic materials, including Si,[13] ZnO,[14] InP,[15] GaN,[16] $Bb_2O_5$,[17] etc., that can be fabricated into NW-based optoelectronic devices. However, high-quality organic and organic–inorganic hybrid NWs with well-defined shape and geometry have rarely been reported, primarily due to limited choice of materials and lack of controllable growth techniques. Recently, the emerging organic–inorganic hybrid perovskite materials, such as $CH_3NH_3PbI_3$ ($MAPbI_3$), $MAPbBr_3$, etc., have demonstrated highly tantalizing optical and electrical characteristics. Specifically, these materials possess tunable energy bandgaps by varying the material compositions, high optical-absorption coefficient, and long carrier life-time on a par with polycrystalline Si.[18,19] These attractive properties certainly make them promising candidates for high-performance NW-based optoelectronic devices.[18,20] Nevertheless, a growth process of these perovskite NWs with high density and high degree of controllability over geometry, i.e., diameter and length, has yet been reported[21,22] and it urgently needed for fundamental investigations of the intriguing properties of these perovskite NWs, as well as exploring their applications for very-large-scale integrated (VLSI) electronics and optoelectronics.

In this work, we report for the first time a vapor–solid–solid reaction (VSSR) process to grow ordered three-dimensional (3D) $MAPbI_3$ NW arrays in nanoengineering templates. This unique VSSR process utilizes lead (Pb) metal nanoclusters at the bottom of vertical nanochannels to initiate high-quality $MAPbI_3$ NW growth. As the nanochannels have largely controllable geometrical factors, namely, periodicity, diameter, and depth, the NW geometry can also be precisely nanoengineered. As a result, the ordered 3D NW arrays can achieve ultrahigh NW density in the range of $4 \times 10^8$–$10^9$ $cm^{-2}$ at a sizable scale of ≈9 $cm^2$. The 3D NW arrays are conspicuously promising for 3D integrated nanoelectronics/optoelectronics. To further demonstrate the technological potency of the perovskite NW arrays, they have been fabricated into proof-of-concept image sensors. Each image sensor consists of 1024 photodiode pixels made of vertical perovskite NWs, and the imaging functionality has been verified by recognizing various optical patterns projected on the sensor. It was found that the NW sensors can respond to dynamic optical input with reasonable speed; thus, the video-capture function of the NW image sensor was also successfully demonstrated. As the diameter of each NW can be as small as hundreds of nanometers and each NW can serve as one sensor pixel, this unique image sensor design can potentially lead to extremely high resolution, approaching the optical diffraction limit.[23] In addition, the fabrication and characterization of flexible image sensors are also demonstrated in this work. The flexible optical sensor arrays can find broad applications for wearable electronics, electronic eyes, multifunctional robotics, and artificial skins, etc.

The overall device structure of a 3D-NW-array-based image sensor can be found in **Figure 1**a. The device consists of six layers of materials from the bottom supporting substrate to the top transparent packaging layer. The key active layer is the 3D $MAPbI_3$ NW array sandwiched by 32 top transparent indium-tin-oxide (ITO) finger electrodes and 32 bottom gold (Au) metal finger electrodes. The magnified schematic of the 3D NW array can also be seen in Figure 1a, showing high-density ordered vertical NWs integrated inside the channels of a nanoengineering template. In this configuration, a vertical device can be formed at the intersection of a pair of top and bottom electrodes, serving as a single pixel of a photodetector that consists of a subarray of NWs. In this work, $32 \times 32$ photodetectors were

Dr. L. Gu, Dr. M. M. Tavakoli, D. Zhang, Q. Zhang, A. Waleed, K.-H. Tsui, Y. Lin, Prof. Z. Fan
Department of Electronic and Computer Engineering
The Hong Kong University of Science and Technology
Clear Water Bay, Kowloon, Hong Kong SAR, China
E-mail: eezfan@ust.hk
Y. Xiao, Prof. J. Wang
Department of Physics
The Hong Kong University of Science and Technology
Clear Water Bay, Kowloon, Hong Kong SAR, China
Prof. L. Liao
Department of Physics and Key Laboratory of Artificial Micro- and Nano-Structures of Ministry of Education
Wuhan University
Wuhan 430072, China

**DOI: 10.1002/adma.201601603**

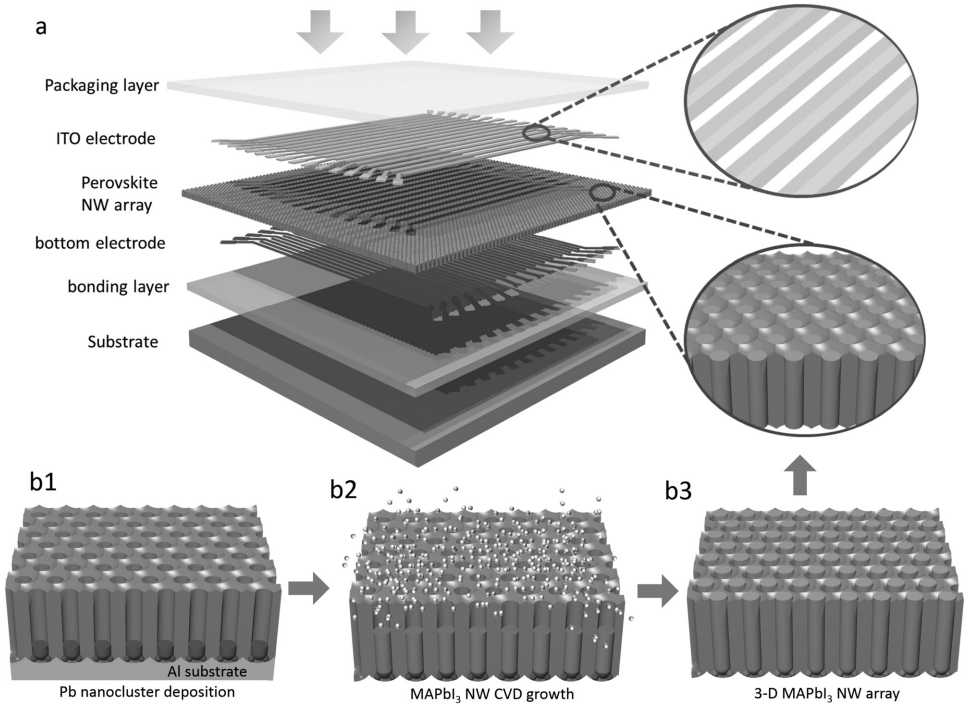


**Figure 1.** a) Layer-by-layer structure of 32 × 32 $MAPbI_3$ NW image sensor. b) Schematic of PAM template assisted growth of vertically aligned, high-density $MAPbI_3$ NW array: b1) Pb in PAM before NW growth. b2) Partial $MAPbI_3$ NW growth in freestanding PAM. b3) Completed $MAPbI_3$ NW growth in PAM.

fabricated in an active area of 1.28 cm × 1.28 cm on a NW array with a size of 3 cm × 3 cm, leading to an image sensor with 1024 imaging pixels. The fabrication process of the device will be introduced in the following paragraphs.

In order to fabricate the key active layer of the perovskite NW array in the device, a 2 μm-thick free-standing porous alumina membrane (PAM) was used as a nanoengineering template to achieve guided NW growth and integration at the same time. In fact, this chemically and mechanically robust PAM can also protect NWs against invasion such as by water and oxygen molecules. A PAM can be fabricated via low-cost electrochemical anodization of aluminum (Al) foil with well-engineered nanochannel periodicity, diameter, and depth (see the Experimental Section). Figure S1a (Supporting Information) shows a top-view scanning electron microscopy (SEM) image of a PAM with hexagonally ordered nanochannels. The perovskite NW VSSR growth process in a PAM is schematically shown in Figure 1b1–b3, the details of which can be found in the Experimental Section. It is worth noting that in many previous reports on $MAPbI_3$ thin-film growth, $PbI_2$ films were deposited first then reacted with MAI to achieve crystalline $MAPbI_3$ films.[24,25] In this work, for the first time, Pb nanoclusters (**Figure 2**a) were used to grow perovskite NWs. Figure 2b and Figure S1b (Supporting Information) show back-scattered-electron (BSE)-mode SEM images of vertical $MAPbI_3$ NWs embedded in the PAM after reaction and Figure 2c shows the top-view SEM image of the same sample, indicating a high degree of NW growth uniformity. The NW length is primarily controlled by the growth time and the amount of Pb deposited in the PAM, as shown in Figure S1c,d (Supporting Information). These results demonstrate the high regularity and excellent control of the NW geometry with this growth approach. It can be seen from Figure S1e (Supporting Information) that, unlike metal-nanoclusters-catalyzed chemical-vapor-deposition NW growth for inorganic NWs,[26,27] there is no trace of the high-contrast metal material on the top of NWs. In fact, in the process of $MAPbI_3$ NW VSSR growth, the role of metal Pb, is clearly as a reactant instead of as a catalyst for conventional inorganic NW growth, which leads to a fundamentally different growth mechanism. The overall reaction can be expressed as:

$$3CH_3NH_3I + Pb \rightarrow CH_3NH_3PbI_3 + 2CH_3NH_2 + H_2 \quad \text{(R1)}$$

This reaction combines two step reactions with $PbI_2$ as an intermediate product (the detailed reaction mechanism can be found in Figure S2 (Supporting Information)). Figure 2c demonstrates a perovskite NW array embedded in a PAM, which was fabricated by nanoimprinting in conjunction with anodization. Note that a perfectly ordered NW array is desirable for applications in which individual NWs are addressable. Meanwhile, a semiordering (Figure S1f, Supporting Information), which can be achieved with anodization without nanoimprinting, is sufficient if a large number of NWs are utilized in parallel for one device, as in the current work.

High-quality organic and inorganic NWs with both good crystallinity and high charge-carrier mobility are desirable for high-performance nanoelectronics/optoelectronics. In order to confirm the quality of the VSSR grown perovskite NWs, systematic characterizations have been performed on

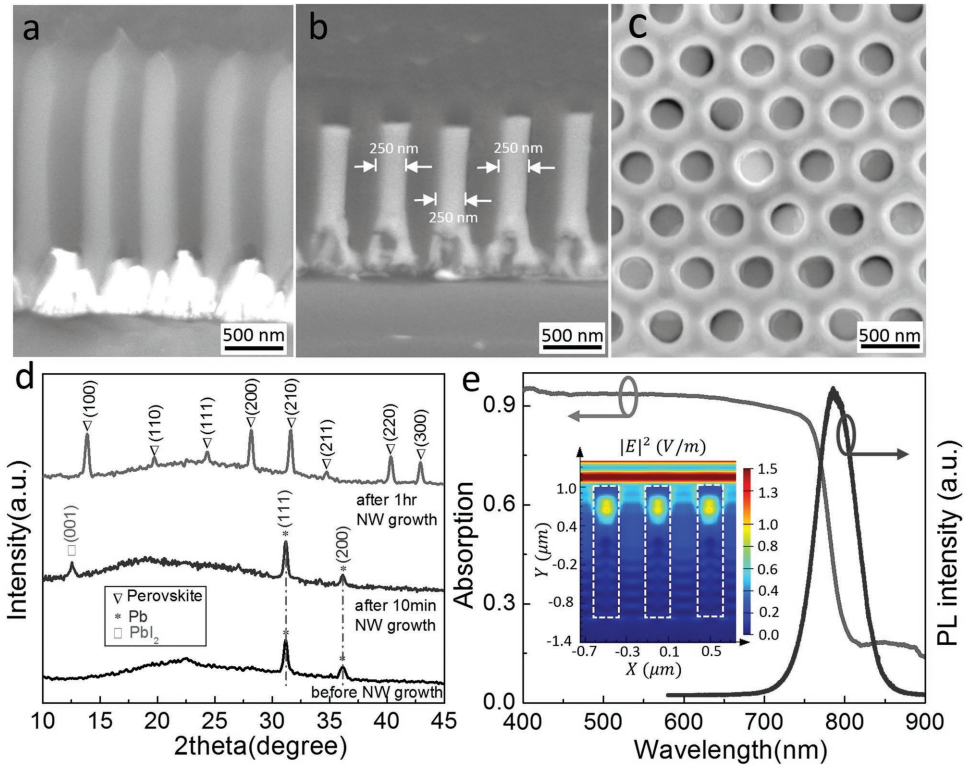


**Figure 2.** a) BSE image of Pb in PAM before NW growth. b) Cross-section and c) top view of $MAPbI_3$ NW in PAM after growth. d) XRD of freestanding PAM before (black curve), after 10 min (blue curve), and 1 h (red curve) NW growth. e) PL (green curve) and UV–vis (purple curve) of $MAPbI_3$ NW array in freestanding PAM. Inset: calculated light distribution inside NWs and PAM.

the material. Figure 2d shows X-ray diffraction (XRD) patterns of a NW array at different growth stages. It can be seen that after a short time (10 min) and incomplete growth, the Pb metal seeds were partially converted to the intermediate product $PbI_2$. When the growth time was prolonged to 1 h till the reaction was completed, the traces of both the Pb and the $PbI_2$ disappeared, and the XRD patterns of final product matched well with the documented results obtained from cubic-phase $CH_3NH_3PbI_3$ thin films.[28,29] This result suggests that the VSSR-growth perovskite NWs in this work have high crystallinity. To further confirm this, individual NWs were also harvested for transmission electron microscopy (TEM) observation, as shown in Figure S3a,c,e (Supporting Information). Selected area electron diffraction (SAED) patterns were obtained and shown in Figure S3b,d,f (Supporting Information). These results indicate that each individual NW is single crystalline with different growth orientations from others, which is due to the amorphous and non-epitaxial nature of the NW growth template of PAM. To shed light on the composition uniformity of NWs, energy-dispersive X-ray spectroscopy (EDX) mapping of the NWs were acquired. As shown in Figure S4 (Supporting Information), NWs embedded in a PAM template show uniform elemental mapping of Pb, I, and C. Also, a free-standing long NW also demonstrated uniform elemental distribution, as shown in Figure S5 (Supporting Information). Note that in these EDX analyses, traces of nitrogen cannot be clearly identified due to the limited detector sensitivity to nitrogen.

Besides structural and compositional analysis, optical characterizations have also been performed on perovskite NWs. Figure 2e shows the measured optical absorption and photoluminescence (PL) spectra of a NW array with 250 nm NW diameter. The optical absorption spectrum together with the Tauc plot shown in Figure S6a (Supporting Information) suggests an optical bandgap of 1.57 eV for the NW array, which is consistent with peak position in the PL spectrum. The inset in Figure 2e shows the electric-field intensity ($|E|^2$) distribution in the NW array with a wavelength of 600 nm. It indicates that the field intensity quickly decays when light enters the NW array from top. The electric-field intensity distributions for 400 and 800 nm wavelengths have also been modeled and are plotted in Figure S6c,e (Supporting Information). It can be observed that short-wavelength light can be efficiently absorbed by the NWs and 800 nm wavelength light can transmit through the NW array. This is consistent with the optical-absorption curve shown in Figure 2e. Meanwhile, time-resolved PL (Figure S6b, Supporting Information) shows an estimated carrier life-time of 14.3 ns, which is comparable with some results from thin-film counterparts with large crystalline grains.[19,30] In addition to NWs with 250 nm diameter, NWs with diameters of 150 and 400 nm have also been fabricated, and their optical properties were measured and modeled, as shown in Figure S7a,b (Supporting Information). As can be seen, the modeled optical-absorption results largely agree with the measured results. Particularly, the NW arrays with all diameters demonstrate better absorption than the planar control sample, this is due to the

nanowire array antireflection and light-trapping effect, which we have reported previously.[31]

The above investigations suggest that 3D perovskite NW arrays have desirable crystallinity and optical properties, and thus can serve as key components for high-performance optoelectronic devices. In this work, proof-of-concept image sensors with 1024 photodiode pixels have been successfully fabricated and demonstrated. The device-fabrication process flow is schematically shown in Figure S8 (Supporting Information). The key step is the transfer process (Figure S8a,b, Supporting Information) to attach the free-standing NW array to a poly(dimethylsiloxane) (PDMS) substrate to facilitate the subsequent device fabrication. The photograph and SEM image of a fully fabricated device on a glass substrate can be seen in Figure S9b,c (Supporting Information). It is worth pointing out that a PAM is a robust template for NW integration that enables various processes on the free-standing NW array. It is conceivable that it will be a great challenge for vertical device fabrication if NW arrays are grown with other methods without the nanoengineering template, for example, the widely used NW epitaxial growth or non-epitaxial growth on supporting substrates.[8,32] More importantly, as shown in Figure S1d (Supporting Information), without nanochannel-guided growth, free-standing NWs have large length and diameter variations, which are highly undesirable for any device applications.

After successful device fabrication, the photoresponse of individual pixels in the image sensor, as well as the imaging function of the sensor device, have been characterized in a systematic fashion. **Figure 3**a schematically shows the configuration of a single-pixel measurement. In the current work, each pixel has footprint of 200 μm × 200 μm with a periodicity of 400 μm and the area of each pixel is determined by the intersection region of a pair of top and bottom electrodes. Considering the density of NWs is $4 \times 10^8$ cm$^{-2}$, there are ≈$1.6 \times 10^5$ NWs

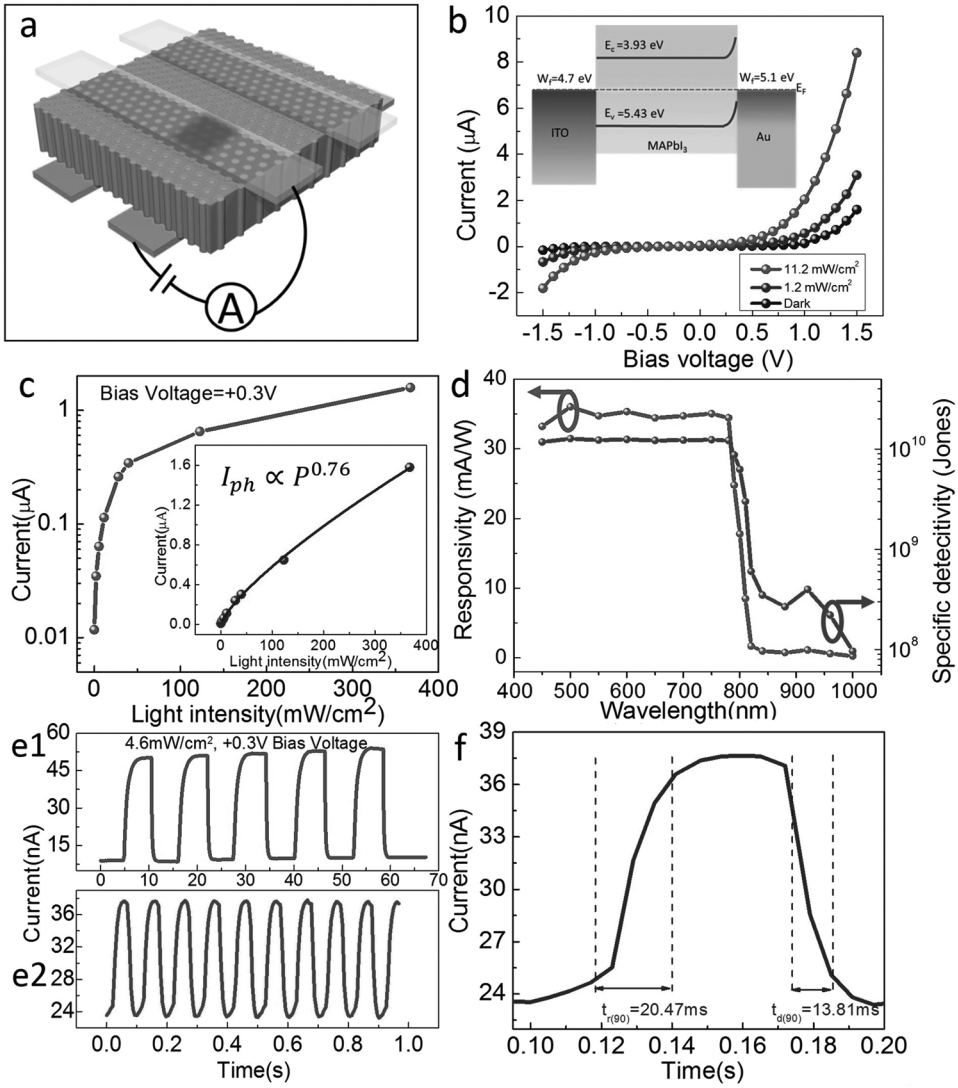


**Figure 3.** a) Schematic of measurement setup. b) *I–V* curves under different illumination intensity (white color light). Inset: band structure of a single-pixel device under zero bias and in the dark. c) Current under exposure to different illumination intensities (white color light). d) Responsivity and specific detectivity measurement under +0.3 V bias voltage. e) Photoresponse to white light (4.6 mW cm$^{-2}$) under 0.1 Hz (e1) and 1 Hz (e2) on/off frequency. f) Response time analysis under light of 4.6 mW cm$^{-2}$ under +0.3 V bias voltage.

in each sensor pixel. As mentioned above, the minimum width of each electrode is limited by the line width of the evaporation shadow mask. In principle, each individual NW can potentially serve as one pixel since all NWs are well isolated by the PAM template. This can lead to extremely high resolution for an image sensor approaching the optical diffraction limit. However, an alternative fabrication technique, such as the nanoimprint lithography method, should be utilized to achieve high-resolution electrode fabrication, while the current device with 1024 pixels is a proof-of-concept to demonstrate feasibility of the device design. Figure 3b shows the current–voltage characteristics (*I*–*V*) of an individual pixel illuminated with different intensity of a halogen light source. The asymmetric nature of the *I*–*V* curves suggests that the pixel device is a typical Schottky photodiode. This can be explained by the asymmetric contact material on top and bottom of the NW array and the resulted band bending at the contact interface, as shown in the inset of Figure 3b. The schematic band alignments for forward and reverse bias and the photocurrent rectification mechanism can be found in Figure S10a,c (Supporting Information). It is worth pointing out that such a current rectification is necessary, in order to suppress cross-talking between neighboring pixels. Figure S11 (Supporting Information) shows the mechanism of cross-talking suppression by using a reverse-biased diode in the potential sneak path. This simple device design addresses the sneak path issue appearing in crossbar memristor-based memory.[33,34] Figure 3c shows the dependence of the photocurrent on the illumination intensity, indicating a sublinear power-law relationship ($I \sim P^{0.76}$) originating from photocarrier saturation at high intensity.[35] In order to investigate the response of the device to different input optical wavelengths, its spectral responsivity ($R_i$) was measured and is shown in Figure 3d. In this case, a low voltage bias of 0.3 V was applied during the measurements. It can be seen that the device has a consistent photoelectric response when the incident optical wavelength is shorter than 780 nm, which is in excellent agreement with the energy bandgap obtained from optical measurements in Figure S6a (Supporting Information). In addition, the specific detectivity of a photodiode device for different optical wavelength illumination is calculated by using the following formula:[14]

$$D^* = \frac{R_i}{\left(2e\frac{I_{dark}}{A}\right)^{1/2}} \quad (1)$$

where $R_i$ is the responsivity, $I_{dark}$ is the dark current, and $A$ is the photodetector area. The result is plotted in Figure 3d. Overall, in the 450–780 nm wavelength range, the NW device demonstrates $\approx 10^{10}$ Jones specific detectivity.

To study the response speed of the single-pixel device, optical input from a halogen lamp with intensity of 4.6 mW cm$^{-2}$ was chopped to 0.1 and 10 Hz frequency and the device photoresponse was measured and shown in Figure 3e1,e2, respectively. Figure 3f shows that the device response is reasonably fast with photocurrent rise time ($t_{rise}$) of 20.47 ms and fall time ($t_{fall}$) of 13.81 ms. This response speed is already faster than that of human-eye pattern recognition (>40 ms); thus, the device can be used for electronic-eye applications.[36] Further improvement of the response speed can be conceivably achieved by reducing the NW length to reduce the charge-carrier transit time and NW resistance, and shrinking the pixel size to reduce the capacitance between the top and bottom electrodes in the future.

After characterization of individual sensor pixels, the full sensor device was measured using the setup shown in **Figure 4**a,b. Specifically, the copper wires connected to the 32 top and 32 bottom electrodes were bonded to the row and column contacts on a printed circuit board (PCB) (Figure 4a). Then two independent 32-to-1 multiplexers were connected to the column and row selections, respectively; thus, a specific pixel can be addressed by selecting the corresponding column and row number (Figure 4b). The multiplexers were interfaced with a computer and a digital source-meter unit so that the photoresponse of the chosen device could be measured and recorded by the computer, as shown in Figure 4b. As all the 1024 pixels can be individually addressed and measured by the computer program, image-sensor function can be examined by projecting optical patterns onto the sensor's active area, then recording and displaying the photocurrent distribution in the program. Before pattern generation and recognition, it is important to verify the consistency of the dark and light current of all the pixels. Figure S12a,b (Supporting Information) demonstrate the dark- and light-current images obtained with 0.2 V bias voltage, respectively. The light-current image was acquired by projecting uniform white light with an intensity of 1.6 mW cm$^{-2}$. It can be clearly seen that all 1024 pixels have a discernible photoresponse. To reconstruct the optical pattern projected on the image sensor, a photocurrent value was converted to grayscale number between 0 and 255. The formula used for grayscale conversion is the following:

$$G = \frac{I_{Meas}}{I_{Full\_scale}} \times 255 = \frac{I_{Light} - I_{Dark}}{I_{Full\_Light} - I_{Dark}} \times 255 \quad (2)$$

In Equation (2), $G$ is the grayscale value, $I_{Meas}$ is the measured photocurrent which is the difference between the light current $I_{Light}$ and the dark current $I_{Dark}$, and $I_{Full\_scale}$ is defined as the difference between the full-light-condition current and the dark current of a pixel. This is, in fact, the result of subtracting Figure S12a (Supporting Information) current mapping from Figure S12b (Supporting Information) current mapping and this parameter defines the dynamic range of the photocurrent. As the results, Figure 4c,d demonstrate the imaged character "H" and a symbol of a heart projected to the image sensor, respectively. Figure S13 (Supporting Information) also shows other characters imaged, including "C," "K," and "2." It can be seen that these symbols can be clearly resolved, indicating the reliable imaging function of the sensor device. Note that the high pixel density and large active area allow our sensor to reconstruct an image without any mechanical movement.[23,37] The absence of slow mechanical movement, together with the reasonably fast sensor response of a single pixel, ensures fast image reconstruction and finally results in the possibility of capturing a video with the device. To demonstrate the video-capture function, a light spot was programmed to move on the surface of the image sensor along a square travel path, as shown in **Figure 5**a,b. Movie S2 (Supporting Information) demonstrates the real-time captured video for the movement of the light spot.

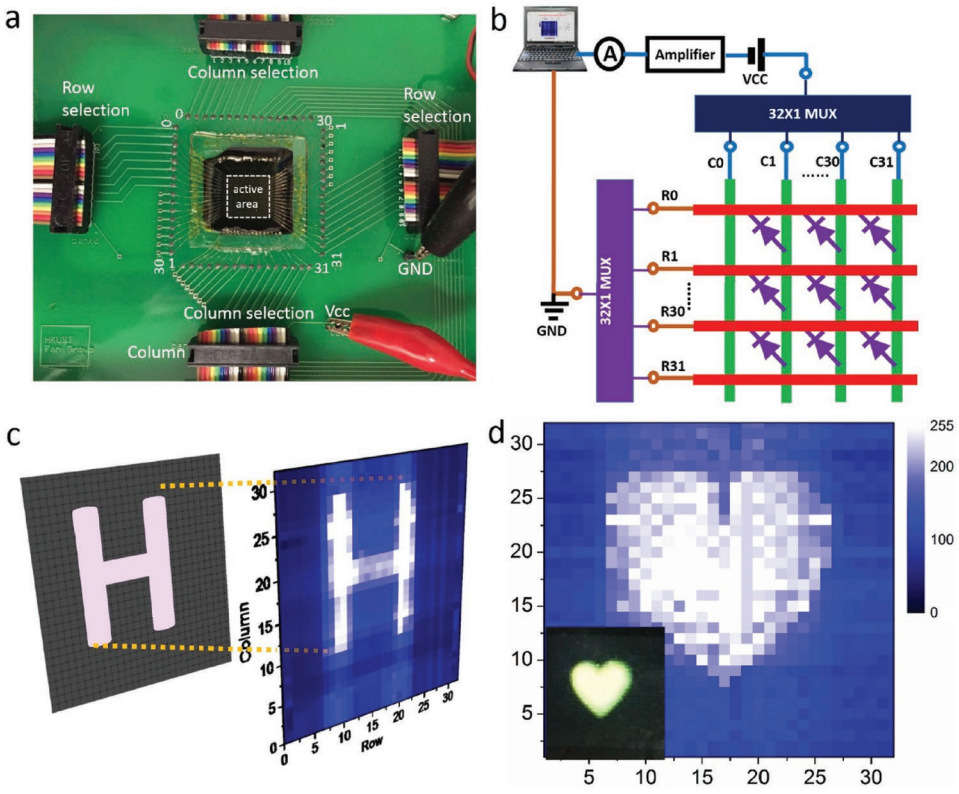


**Figure 4.** a) Photograph of an image sensor mounted on a printing circuit board. b) Schematic of measurement setup. c) Original and imaged letter ("H"). d) Original and imaged love heart pattern.

As shown in Figure S8 (Supporting Information), the NW-array transfer process starts from a free-standing NW array and it does not have stringent requirements on the supporting substrate, as long as it has acceptable flatness. In the most part of our work, glass substrates were used for the convenience, as shown in Figure S9b (Supporting Information). In fact, the 2 µm-thick NW array grown in PAM has excellent mechanical flexibility. As shown in Movie S1 (Supporting Information), the PAM film can be unrolled easily without being damaged. This indicates the possibility of fabricating flexible image sensors with perovskite NW arrays, which can find applications in wearable and flexible electronics, artificial skin, electronic eyes, etc. In experiments, we have also fabricated sensor devices on thin and flexible poly(ethylene terephthalate) (PET) substrates and, moreover, this PET substrate can be peeled off from device to further improve the flexibility. A representative flexible device can be found in Figure S14a (Supporting Information) and the schematic of the device structure is shown in Figure S14b (Supporting Information). To examine the functionality of the flexible device, a circular light beam is projected to the device, as shown in Figure 5c,d. As the device has a certain curvature, the captured image was corrected and shown in Figure 5e. The details of device-bending-related image correction can be found in Figure S15 (Supporting Information).

In summary, here we report a unique fabrication process to form large-scale, 3D, high-density arrays of lead halide perovskite NWs with well-engineered geometry. The high regularity of the NW array leads to the possibility of having electrically addressable individual NWs, which enables potential applications for VLSI electronics and optoelectronics. As a proof-of-concept, image sensors with 1024 pixels have been fabricated and their capability of capturing still images and video has been well demonstrated. In conjunction with the intriguing electrical and optical properties of perovskite materials, such 3D NW arrays may find a broad spectrum of applications for optoelectronic devices, such as solar cells, photodetectors, light-emitting diodes, etc. The unique NW integration approach here, together with NW geometrical and compositional tenability, may lead to new functionality and inspire novel device design in the future.

## Experimental Section

*PAM Fabrication*: The PAMs were prepared through a two-step anodization of high-purity Al foils reported previously. Briefly, Al foil with a thickness of 0.25 mm was cut into 3 cm × 4 cm pieces and cleaned in acetone and isopropyl alcohol. The sheets were then electrochemically polished in an acidic solution (25 vol% $HClO_4$ mixed with 75 vol% absolute $CH_3CH_2OH$) for 5 min under 19 V at 10 °C. After polishing, to fabricate PAM with perfect hexagonally ordered nanochannels, the Al sheets were imprinted using silicon mold (hexagonally ordered pillar array with height of 200 nm, diameter of 200 nm, and pitch of 500 nm) with a pressure of ≈$2 \times 10^4$ N $cm^{-2}$ to initiate the perfectly ordered PAM growth. The Al substrates were then immersed in solution (deionized water:ethylene glycol:$H_3PO_4$ = 200:100:0.5, by volume) for anodization under a 200 V d.c. bias, 10 °C for 10 min. Afterward, the first anodization layer was etched away in a mixture of phosphoric acid (6 wt% $H_3PO_4$ and 1.8 wt% $CrO_3$) at 98 °C for 10 min. After etching, the second anodization was carried

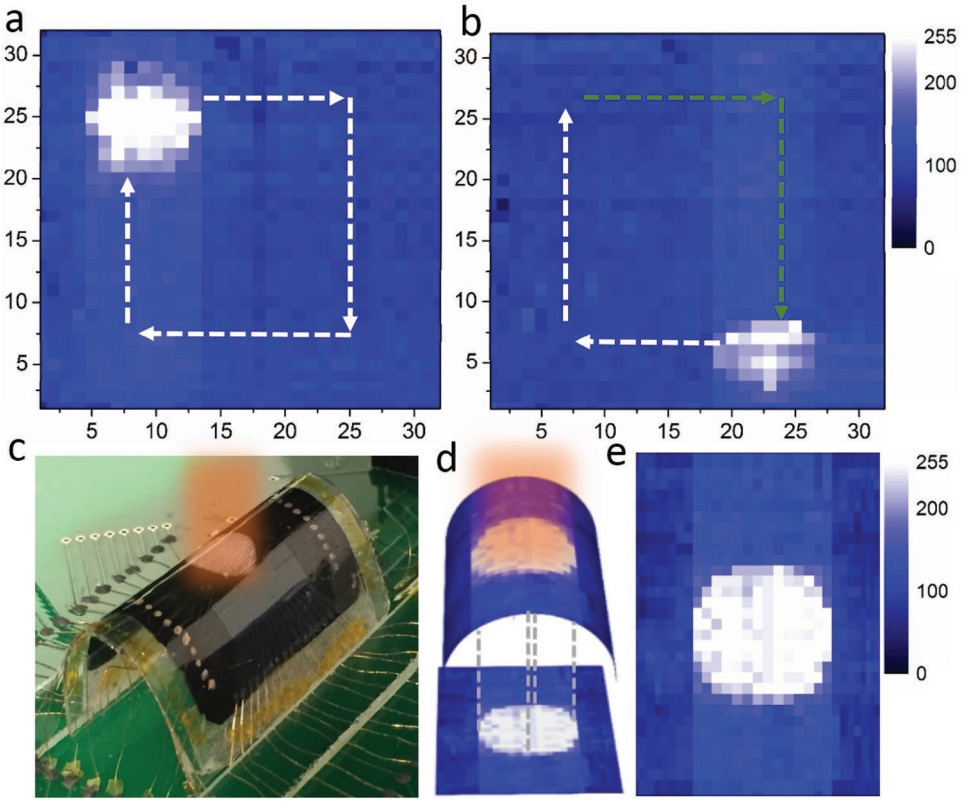


**Figure 5.** Video-capture function demonstration and flexible NW array image sensor. a) A light spot at the starting point of its moving path indicated by the dashed line arrows. b) The light spot halfway along its moving path. c) Photograph of a bent flexible sensor device mounted on a PCB for measurement. d) Imaged circular pattern on bent image sensor and its projection plane. e) The acquired circular light pattern image after correction.

out under the same conditions for 40 min to obtain ≈2 µm thick PAM. Finally, the template was further etched in a $H_3PO_4$ aqueous solution (5 wt%, 52 °C) for 10 min to widen the channel diameter to 230 nm. The fabrication of the semiordered PAM followed the same process, except that the imprinting process was skipped, and the first anodization time was prolonged to 10 h to promote natural hexagonal ordering.

*Barrier Thinning and Pb Electrodeposition*: To facilitate the electrochemical deposition of Pb nanoclusters, a voltage-ramping-down process was carried out to thin down the barrier layer at the bottom of PAM nanochannels. This process was in fact another anodization step carried out in 0.2 M $H_3PO_4$ solution at room temperature controlled by a computer program and a Keithley 2400. In the beginning, the Keithley 2400 was set in voltage-source mode and the anodization voltage was gradually ramped up to 160 V and the electric current $I_0$ was recorded. Then the Keithley 2400 was switched to current-source mode and the current was set to $I_0/2$. A gradual decrease of current was then observed. When the current declining rate was slower than 3 V $min^{-1}$, the voltage measured was around 80 V. The current was then set to $I_0/4$ so that the voltage declining process was expedited. When the voltage reached 4 V, the process was terminated. Typically, the entire process took about 20 min.

After barrier thinning, Pb was electrochemically deposited at the bottom of PAM channels in a three-electrode system with an alternating-current method by using a potentiostat (SG 300, Gamry Instruments). The electrolyte was prepared by dissolving 1.7 g of lead(II) chloride ($PbCl_2$) and 25 g of trisodium citrate ($Na_3C_6H_5O_7$) in 100 mL of water under vigorous stirring. A 60 Hz sinusoidal voltage was applied for 10 min, and the amplitude was adjusted from 3.4 to 9 V to maintain a peak current density of 2.2 mA $cm^{-2}$ at the negative deposition cycle. After deposition, the chip was rinsed by deionized water for several times to remove the adsorbed chemicals. The achieved Pb was ≈200 nm thick at the bottom of PAM.

*Preparation of Free-Standing PAMs*: 2 µm-thick free-standing PAMs with Pb nanoclusters embedded was prepared by etching away the Al substrate in saturated $HgCl_2$ aqueous solution. To protect the electrochemically deposited Pb from being etched away, the PAM/Al chip was first covered by a layer of crystalbond (509, Ted Pella, Inc.), which was an adhesive that had a flowing point of 120 °C. Afterward, the whole chip was kept in saturated $HgCl_2$ solution vertically for ≈1 h to etch away Al substrate. Then, the sample was transferred into acetone to remove the crystalbond. After ≈30 min, the free-standing PAM was collected by a clean Si chip and transferred to fresh acetone solution for another 20 min to clean up the residual of crystalbond. Eventually, the PAM was baked at 80 °C for 2 min and it was naturally separated from the Si substrate.

*Preparation of MAI Powder*: Methylamine iodide (MAI) was synthesized by reaction of 27.8 mL of methylamine (33 wt% in ethanol, Sigma–Aldrich) and 30 mL of hydroiodic acid (57 wt% in water, Sigma–Aldrich) in a 250 mL three-neck flask at 0 °C for 2 h. Hydroiodic acid was dropped into MAI solution during stirring. A white precipitate was harvested from the solution using a rotary evaporator at 50 °C. The MAI powder was dissolved in absolute ethanol and precipitated by adding diethyl ether to the solution. After filtration, the process was repeated several times and, finally, the white powder was attained and dried at 60 °C in a vacuum oven overnight.

*Growth of $MAPbI_3$ NWs*: The $MAPbI_3$ NWs were obtained through the reaction between Pb and MAI vapor. The growth process was carried out in a 2 in. two-zone tube furnace (OTF 1200X-II, MTI). The MAI powder was kept at the bottom of a glass bottle (diameter of 4 cm, length of 10 cm) while a free-standing PAM/Pb chip was fixed on a Si chip and placed at its opening end. A second bottle with a smaller diameter was placed beside this bottle, with its opening end inserting into the first bottle to obtain ≈1 cm overlap. This enclosed configuration helped to

maintain the high MAI vapor pressure inside. During reaction, the PAM temperature was controlled at 205 °C and the MAI powder temperature was set at ≈180 °C. A typical growth process lasted for 6 h under atmospheric pressure with 300 sccm continuous argon flow.

*Fabrication of Image-Sensor Devices*: The surface of a PAM with grown NWs was cleaned by ion milling at a 100 V accelerating voltage followed by 10 min annealing at 205 °C to repair potential structural damage caused by the argon beam. Afterward, the PAM was gently transferred to a PDMS substrate. The free-standing PAM unrolled itself naturally on the PDMS substrate as shown in Video S1 (Supporting Information). Then, 100 nm-thick Au finger electrodes were evaporated on the PAM using a stainless-steel shadow mask. The typical electrode width and gap were both 200 μm. Then, thin copper wires (60 μm in diameter) were bonded to each individual electrode by carbon paste manually. The whole chip was then bonded to a glass substrate using optical epoxy (NOA81, Norland). After UV curing the epoxy, the PDMS substrate was slowly peeled off from the device. The reverse side of the PAM was then cleaned by ion milling at 500 V acceleration voltage for 1 h. This step also removed the remaining alumina barrier layer for reliable electrical contact on top. Thereafter, 100 nm-thick ITO finger electrodes were sputtered on top using the same shadow mask. The top and bottom electrodes were orthogonalized to each other to form 1024 intersections. Thin copper wires were also bonded to top ITO electrodes manually. Afterward, three layers of poly(methyl methacrylate) (950 A2) were spin coated on top of the device to passivate it. To fabricate a flexible device, a 2 mm thick polycarbonate film was used instead of the glass slide. After poly(methyl methacrylate) spin coating, the ITO electrode side was bonded to another PDMS substrate by epoxy. After epoxy curing and peeling of the polycarbonate film and PDMS, the whole device was encapsulated inside of two epoxy layers, as shown in Figure S14a,b (Supporting Information).

*Image-Sensor Characterization*: The image-sensor devices were characterized by using a home-built system consisting of two multiplexers, a preamplifier, a laptop computer, and the Labview program. The schematic of the system can be found in Figure 4b. Specifically, a Keithley 2400 was used to provide the bias voltage. A Keithley 485 picoammeter worked as a preamplifier, which essentially converted low current into voltage. The voltage meter (PXI4130, National Instruments), together with a multiplexer (PXI2530B, National Instruments), was installed inside a chassis box (PXI1031, National Instruments). During measurement, an image-sensor device was placed inside of a grounded aluminum box to reduce electrical noise. The whole system was controlled by a home-built Labview computer program. To carry out the measurements, various optical patterns were generated by PowerPoint slides and projected onto the device by using a projector through a window on the aluminum box. A convex lens was used to focus the pattern and different neutral-density filters were inserted between the projector and image sensor to tune the light intensity.

*Optical Simulation*: Finite-difference time-domain (FDTD) method was utilized to study the optical properties of the perovskite nanowire hexagonal arrays of 500 nm pitch and 150, 250, and 400 nm diameters. All the nanowires were 2 μm long and were fully embedded in 2 μm thick PAM thin film. The light source with wavelength range 400–900 nm was located at $z = 1.5$ μm and propagated downward. Periodic boundary conditions were applied on the $x$ and $y$ directions and perfect matched layers were applied on thez direction. Electric field square ($|E|^2$) was studied to indicate the light intensity. The absorption spectra of different geometries were also calculated and compared.

## Supporting Information

Supporting Information is available from the Wiley Online Library or from the author.

## Acknowledgements

L.G. and M.M.T. contributed equally to this work. This work was supported by the General Research Fund (projects 612113 and T23-407/13N-2) from the Hong Kong Research Grant Council, the Hong Kong Innovation and Technology Fund (ITS/362/14FP) from the Innovation and Technology Commission. The authors also acknowledge the support from the Center for 1D/2D Quantum Materials and the State Key Laboratory on Advanced Displays and Optoelectronics at HKUST.

Received: March 23, 2016
Revised: July 17, 2016
Published online: September 20, 2016

[1] Y. Cui, Z. Zhong, D. Wang, W. U. Wang, C. M. Lieber, *Nano Lett.* **2003**, *3*, 149.
[2] S. Chuang, Q. Gao, R. Kapadia, A. C. Ford, J. Guo, A. Javey, *Nano Lett.* **2012**, *13*, 555.
[3] Z. Fan, J. C. Ho, Z. A. Jacobson, R. Yerushalmi, R. L. Alley, H. Razavi, A. Javey, *Nano Lett.* **2008**, *8*, 20.
[4] C. Pan, L. Dong, G. Zhu, S. Niu, R. Yu, Q. Yang, Y. Liu, Z. L. Wang, *Nat. Photonics* **2013**, *7*, 752.
[5] S.-H. Lee, Y. Jung, R. Agarwal, *Nat. Nanotechnol.* **2007**, *2*, 626.
[6] F. Xiong, M.-H. Bae, Y. Dai, A. D. Liao, A. Behnam, E. A. Carrion, S. Hong, D. Ielmini, E. Pop, *Nano Lett.* **2013**, *13*, 464.
[7] Z. Fan, J. G. Lu, *Appl. Phys. Lett.* **2005**, *86*, 123510.
[8] W. Wu, X. Wen, Z. L. Wang, *Science* **2013**, *340*, 952.
[9] J. H. Lee, A. Zhang, S. You, C. M. Lieber, *Nano Lett.* **2016**, *16*, 1509.
[10] J. R. D. Retamal, C.-Y. Chen, D.-H. Lien, M. R. Huang, C.-A. Lin, C.-P. Liu, J.-H. He, *ACS Photonics* **2014**, *1*, 354.
[11] Z. Fan, H. Razavi, J.-W. Do, A. Moriwaki, O. Ergen, Y.-L. Chueh, P. W. Leu, J. C. Ho, T. Takahashi, L. A. Reichertz, S. Neale, K. Yu, M. Wu, J. W. Ager, A. Javey, *Nat. Mater.* **2009**, *8*, 648.
[12] S. Brittman, Y. Yoo, N. P. Dasgupta, S.-I. Kim, B. Kim, P. Yang, *Nano Lett.* **2014**, *14*, 4665.
[13] L. Cao, J. S. White, J.-S. Park, J. A. Schuller, B. M. Clemens, M. L. Brongersma, *Nat. Mater.* **2009**, *8*, 643.
[14] X. Liu, L. Gu, Q. Zhang, J. Wu, Y. Long, Z. Fan, *Nat. Commun.* **2014**, *5*, 4007.
[15] J. Wallentin, N. Anttu, D. Asoli, M. Huffman, I. Åberg, M. H. Magnusson, G. Siefer, P. Fuss-Kailuweit, F. Dimroth, B. Witzigmann, H. Q. Xu, *Science* **2013**, *339*, 1057.
[16] X. Dai, A. Messanvi, H. Zhang, C. Durand, J. Eymery, C. Bougerol, F. H. Julien, M. Tchernycheva, *Nano Lett.* **2015**, *15*, 6958.
[17] X. Fang, L. Hu, K. Huo, B. Gao, L. Zhao, M. Liao, P. K. Chu, Y. Bando, D. Golberg, *Adv. Funct. Mater.* **2011**, *21*, 3907.
[18] H. Zhu, Y. Fu, F. Meng, X. Wu, Z. Gong, Q. Ding, M. V. Gustafsson, M. T. Trinh, S. Jin, X.-Y. Zhu, *Nat. Mater.* **2015**, *14*, 636.
[19] S. D. Stranks, G. E. Eperon, G. Grancini, C. Menelaou, M. J. Alcocer, T. Leijtens, L. M. Herz, A. Petrozza, H. J. Snaith, *Science* **2013**, *342*, 341.
[20] W. Deng, X. Zhang, L. Huang, X. Xu, L. Wang, J. Wang, Q. Shang, S.-T. Lee, J. Jie, *Adv. Mater.* **2016**, *28*, 2201.
[21] A. B. Wong, M. Lai, S. W. Eaton, Y. Yu, E. Lin, L. Dou, A. Fu, P. D. Yang, *Nano Lett.* **2015**, *15*, 5519.
[22] Y. Fu, H. Zhu, A. Schrader, D. Liang, Q. Ding, P. Joshi, L. Hwang, X.-Y. Zhu, S. Jin, *Nano Lett.* **2016**, *16*, 1000.
[23] C. Jiang, J. Song, *Adv. Mater.* **2015**, *27*, 4454.
[24] Y. Fu, F. Meng, M. B. Rowley, B. J. Thompson, M. J. Shearer, D. Ma, R. J. Hamers, J. C. Wright, S. Jin, *J. Am. Chem. Soc.* **2015**, *137*, 5810.
[25] M. Liu, M. B. Johnston, H. J. Snaith, *Nature* **2013**, *501*, 395.
[26] Z. Fan, D. Dutta, C.-J. Chien, H.-Y. Chen, E. C. Brown, P.-C. Chang, J. G. Lu, *Appl. Phys. Lett.* **2006**, *89*, 213110.
[27] L. Gu, X. Liu, K. Kwon, C.-C. La, M. H. Lee, K. Yu, Y.-L. Chueh, Z. Fan, *Nanoscale* **2013**, *5*, 7213.

[28] T. Baikie, Y. Fang, J. M. Kadro, M. Schreyer, F. Wei, S. G. Mhaisalkar, M. Graetzel, T. J. White, *J. Mater. Chem. A* **2013**, *1*, 5628.
[29] J. Burschka, N. Pellet, S.-J. Moon, R. Humphry-Baker, P. Gao, M. K. Nazeeruddin, M. Grätzel, *Nature* **2013**, *499*, 316.
[30] M. M. Tavakoli, L. Gu, Y. Gao, C. Reckmeier, J. He, A. L. Rogach, Y. Yao, Z. Fan, *Sci. Rep.* **2015**, *5*, 14083.
[31] Z. Fan, R. Kapadia, P. W. Leu, X. Zhang, Y.-L. Chueh, K. Takei, K. Yu, A. Jamshidi, A. A. Rathore, D. J. Ruebusch, M. Wu, A. Javey, *Nano Lett.* **2010**, *10*, 3823.
[32] H. Park, Y. Dan, K. Seo, Y. J. Yu, P. K. Duane, M. Wober, K. B. Crozier, *Nano Lett.* **2014**, *14*, 1804.
[33] E. Linn, R. Rosezin, C. Kügeler, R. Waser, *Nat. Mater.* **2010**, *9*, 403.
[34] M. A. Zidan, H. Omran, R. Naous, A. Sultan, H. A. Fahmy, W. D. Lu, K. N. Salama, *Sci. Rep.* **2016**, *6*, 18863.
[35] A. Rose, *Concepts in Photoconductivity and Allied Problems*, Krieger, New York **1978**.
[36] R. Näsänen, H. Ojanpää, T. Tanskanen, J. Päällysaho, *Exp. Brain Res.* **2006**, *172*, 464.
[37] H. C. Ko, M. P. Stoykovich, J. Song, V. Malyarchuk, W. M. Choi, C.-J. Yu, J. B. Geddes III, J. Xiao, S. Wang, Y. Huang, J. A. Rogers, *Nature* **2008**, *454*, 748.